Computers and Concrete, *Vol.15, No.4 (2015) 563-588*
DOI: http://dx.doi.org/10.12989/cac.2015.15.4.563

Influence of axial load and loading path on the performance of R.C. bridge piers

Fouad Kehila[*1,2] , Hakim Bechtoula[1a] and Djillali Benaouar[2b]

[1]*National Earthquake Engineering Research Center CGS, 01 Rue Kaddour RAHIM, BP 252, Hussein Dey, Algiers, Algeria*
[2]*Bab Ezzouar University of Science & Technology, USTHB BP32, El Alia, Bab Ezzouar, Algiers, Algeria*

(*Received July 21, 2014, Revised October 4, 2014, Accepted February 6, 2015*)

Abstract. Piers are the most vulnerable part of a bridge structure during an earthquake event. During Kobe earthquake in 1995, several bridge piers of the Hanshin Expressway collapsed for more than 600m of the bridge length. In this paper, the most important results of an experimental and analytical investigation of ten reinforced concrete bridge piers specimens with the same cross section subjected to constant axial (or variable) load and reversed (or one direction) cycling loading are presented. The objective was to investigate the main parameters influencing the seismic performance of reinforced concrete bridge piers. It was found that loading history and axial load intensity had a great influence on the performance of piers, especially concerning strength and stiffness degradation as well as the energy dissipation. Controlling these parameters is one of the keys for an ideal seismic performance for a given structure during an eventual seismic event.
Numerical models for the tested specimens were developed and analyzed using SeismoStruct software. The analytical results show reasonable agreement with the experimental ones. The analysis not only correctly predicted the stiffness, load, and deformation at the peak, but also captured the post-peak softening as well. The analytical results showed that, in all cases, the ratio, experimental peak strength to the analytical one, was greater than 0.95.

Keywords: bridge piers; reinforced concrete; performance; cyclic loading; damage; energy dissipation

1. Introduction

Concrete bridges are very important structures (Á lvarez *et al*. 2012; Wei and Wu 2013) serving public transportation. Frequently, earthquakes cause severe damage to bridges in many countries. Bridge must be designed to withstand earthquakes without collapse. Piers in particularly, must be designed with adequate strength and ductility in order to dissipate the seismic energy through inelastic deformation. Since the deterioration in member capacity, which can also be quantified with the deterioration in energy absorption and dissipation capacity, is a composition of stiffness degradation, strength degradation and pinching, all relevant parameters such as axial load ratio, reinforcement ratio, shear span ratio, loading history, concrete strength, bond strength etc. affect the member response under random dynamic excitations (Acun 2010; Acun and Sucuoglu 2012).

∗Corresponding author, Ph.D. Candidate, E-mail: fouad.kehila@gmail.com
[a]Head of Department, Ph.D., E-mail: bechhakim@gmail.com
[b]Professor., E-mail : dbenouar@usthb.dz

 ISSN: 1598-8198 (Print), 1598-818X (Online)

Some investigations have been carried out in the past to investigate the inelastic behavior of reinforced concrete bridge piers (Chang 2010; Han *et al*. 2013; Iranmanesh and Ansari 2013) subjected to strong earthquakes, and specimens simulating reinforced concrete bridge piers have been tested under various loading conditions such as static and dynamic cyclic loading.

Among all, within the scope of this study, a special emphasis has been given to the effect of loading history as well as the effect of axial load. Galal and Ghobarah (2003) investigated the effect of variable axial load amplitude and pattern on strength, stiffness and deformation capacity of reinforced concrete members. Knowing the fact that the magnitude of axial load has an effect on sectional moment capacity, they verified that the axial load history should be identified clearly to assess the response of column members. Sezen and Moehle (2006) studied the effect of axial load and lateral load history and magnitude on member response, concluding that a new definition should be done for performance assessment of reinforced concrete columns depending on their axial load level since it is a crucial parameter on failure mode. They also investigated the influence of loading pattern on deformation capacity of columns and concluded that under constant axial load, deformation capacity of tested specimens under monotonic loading are greater than the ones tested under cyclic loading. Bechtoula *et al*. (2005) tested small-scale and large-scale reinforced concrete specimens designed for flexure to assess the effects of parameters such as axial load and loading pattern (uni-direction, square, circular), finding out that the intensity of applied load has a minor effect on strength deterioration for specimens tested under uni-directional horizontal loading compared to the specimens tested under other loading patterns. They also showed that the equivalent viscous damping has an increasing trend with the increase in axial load. Sheikh tested fifty-six specimens under monotonic loading and used the results of experimental testing (Sheikh 1978) to present a numerical procedure for predicting the behavior of plastic hinge. The columns had a concrete strength in the range from 31.3 MPa to 40.9 MPa. In a study by Cheok and Stone (1990), six circular concrete bridge columns of scale 1:6 were subjected to quasi-static cyclic loading to study their behavior while varying some of their parameters such as the aspect ratio, axial load, and the type of material. The concrete strength for the columns was 27.6 MPa. Some researchers have undertaken full-scale dynamic testing of bridges but mainly limited to ambient vibration testing and/or forced vibration testing using external exciters for the purpose of determining the natural periods, modal shapes and modal damping ratios (Salawu and Williams 1993). Sheikh and Toklucu tested twenty-seven reinforced concrete columns under monotonic axial compression with concrete strength around 35 MPa (Sheikh and Toklucu 1993). In their study, they investigated the effect of various parameters such as the amount and type of lateral steel, spacing of lateral steel and specimen size. El-Bahy *et al*. (1999a) tested twelve circular concrete bridge columns of scale 1:4 under cyclic loading. The concrete strengths varied between 36 to 40MPa. The purpose of this testing was to study the cumulative damage in concrete bridge piers designed with AASHTO specifications. The researchers have also conducted a study of the effect of variable amplitude loading on the column response (El-Bahy *et al*. 1999b). In Japan, Kawashima and others have tested around 50 concrete bridge columns using quasi-static methods. The purpose of testing has been related to various objectives such as the effect of loading hysteresis on ductility, effect of interlocking ties on strength and ductility, verifying plastic hinge lengths, etc. The concrete strength of these columns varied between 20 and 37 MPa (Takemura and Kawashima 1997; Kawashima *et al*. 2000; Fujikura *et al*. 2000). Full-scale testing of five concrete bridge columns was undertaken by Bae and Bayrak (2008) to study their seismic performance. The cyclic testing was performed under a constant axial load. The concrete strengths of the columns were between 30 to 43 MPa. Two large-scale tests on bridges on shake tables were conducted for

verification of bridge condition assessment (Chen *et al*. 2008). One test was on a two-column reinforced bridge bent and other was on a three-column bent. Mullapudi and Ayoub (2013) described the implementation of a three-dimensional (3D) concrete constitutive model for fiber-based analysis of RC members subjected to combined loadings including torsion. The proposed model was formulated to address the interaction between the axial force, bidirectional shear, biaxial bending, and torsion. The shear mechanism along the beam was modeled using a Timoshenko beam approach with 3D frame elements with arbitrary cross-sectional geometry. The model considered the 3D equilibrium, compatibility, and constitutive laws of materials at the section and structural level. The emphasis of their work was on evaluation of the effect of the different stress states on the global and local behavior of the member. Seismic performance of hollow reinforced concrete and prestressed concrete bridge columns were assessed by Tae *et al*. (2012) to provide data for developing improved seismic design criteria. By using a sophisticated nonlinear finite element analysis program, the accuracy and objectivity of the assessment process can be enhanced. A computer program, RCAHEST (Reinforced Concrete Analysis in Higher Evaluation System Technology), was used to analyze reinforced concrete and prestressed concrete structures. Tensile, compressive and shear models of cracked concrete and models of reinforcing and prestressing steel were used to account for the material nonlinearity of reinforced concrete and prestressed concrete. The smeared crack approach was incorporated. The proposed numerical method for the seismic performance assessment of hollow reinforced concrete and prestressed concrete bridge columns was verified by comparing it with the reliable experimental results.

In this paper, experimental and analytical results of ten reinforced concrete bridge piers are presented. The specimens are those available in the data bank of Professor Kawashima from Tokyo Institute of Technology, Japan (Sakai and Kawashima 2002).

2. Specimens and test set-up

2.1 Materials characteristics

The specimens used for this investigation were taken from Sakai and Kawashima data bank. Fig. 1 shows the geometrical characteristics and the steel arrangement of the tested specimens. Material characteristics and applied axial load intensity are summarized in Table 1. The six specimens, tp001 to tp006, had an effective height of 1.245m tall with a cross section of 400 mm × 400 mm as shown in Fig. 1(a). Twenty D13 were provided for longitudinal bars, and D6 bars with 70 mm interval for ties. The longitudinal reinforcement ratio and the volumetric tie reinforcement ratio were 1.58% and 0.57%, respectively. Concrete compressive strength varied between 33.2 and 36.8MPa, see Table 1. A constant axial force of 156.8kN was applied, resulting to an axial stress of 0.98MPa in the pier. Based on calculation, the initial yield displacement δ_y is 6.0 mm, which is nearly equal to 0.48 % drift.

The steel arrangement of the other four specimens called tp031 to tp034 is shown in Fig. 1(b) The specimens had an effective height of 1.35 m tall with square cross section of 400 mm × 400 mm. Twenty D13 bars and D6 bars with an interval of 50mm was provided for longitudinal and transversal reinforcement, respectively. The yield strength of D13 and D6 bars were, respectively, 374MPa and 363MPa. The longitudinal reinforcement ratio and the volumetric tie reinforcement ratio were 1.58% and 0.79%, respectively. The concrete compressive strength was 23.0MPa.

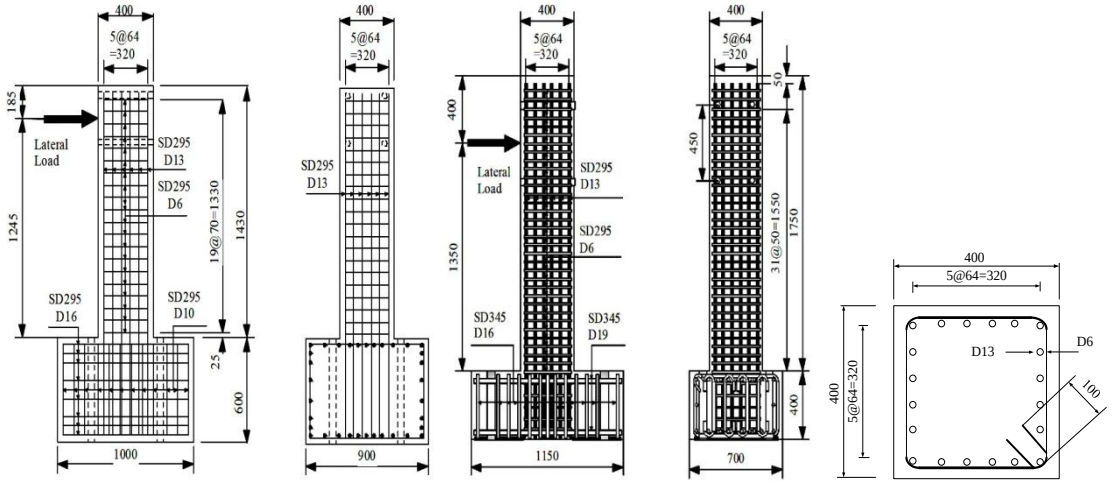

(a) tp001 to tp006 (b) tp031 to tp034

Fig. 1 Geometrical characteristics of the specimens

Table 1 Properties of test specimens

Specimen	tp001	tp002	tp003	tp004	tp005	tp006
Section size (mm)	400×400 (square)					
Effective height (mm)	1245					
Effective depth (mm)	360					
Aspect ratio	3.46					
Longitudinal reinforcement ratio %	1.58					
Volumetric ratio of tie %	0.57					
Cylinder strength of concrete (Mpa)	35.9	35.7	34.3	33.2	36.8	35.9
Longitudinal reinforcement / (yield strength)	SD295 D13 / 363MPa					
Tie reinforcement / (yield strength)	SD295 D6 / 368MPa					
Axial Force (kN) at the bottom	157					
Specimen	tp031	tp032	tp033	tp034		
Section size (mm)	400×400 (square)					
Effective height (mm)	1350					
Effective depth (mm)	360					
Aspect ratio	3.75					
Longitudinal reinforcement ratio %	1.58					
Volumetric ratio of tie %	0.79					
Cylinder strength of concrete (Mpa)	22.9	23.0	22.9	23.0		
Longitudinal reinforcement / (yield strength)	SD295 D13 / 374MPa					
Tie reinforcement / (yield strength)	SD295 D6 / 363MPa					
Axial Force (kN) at the bottom	470 constant	-170 constant	-10~310 varying	-170~420 varying		

2.2 Loading histories

The loading program included a combination of a constant, variable axial load and cyclic lateral displacement. Fig. 2 shows the cyclic loading history, which was based on the lateral displacement pattern of increasing yield displacement. Subsequent cycles during the test were conducted in displacement control. Six loading hysteresis, as shown in Fig. 2, were used for specimens tp001 to tp006. Types 1, 2, and 3 are for investigating the effect of number of load cycles. Type 4 represents a stepwise decrease loading. Type 5 and Type 6 are for studying residual displacement in one direction.

Fig. 3 show the cyclic loading history used for specimens tp031 to tp034, the bridge piers stepwise loaded in the lateral direction under four different vertical loads: (tp031) constant compression axial load corresponding to normalized axial load (N/f'_cA_g) of 12.8%; (tp032)

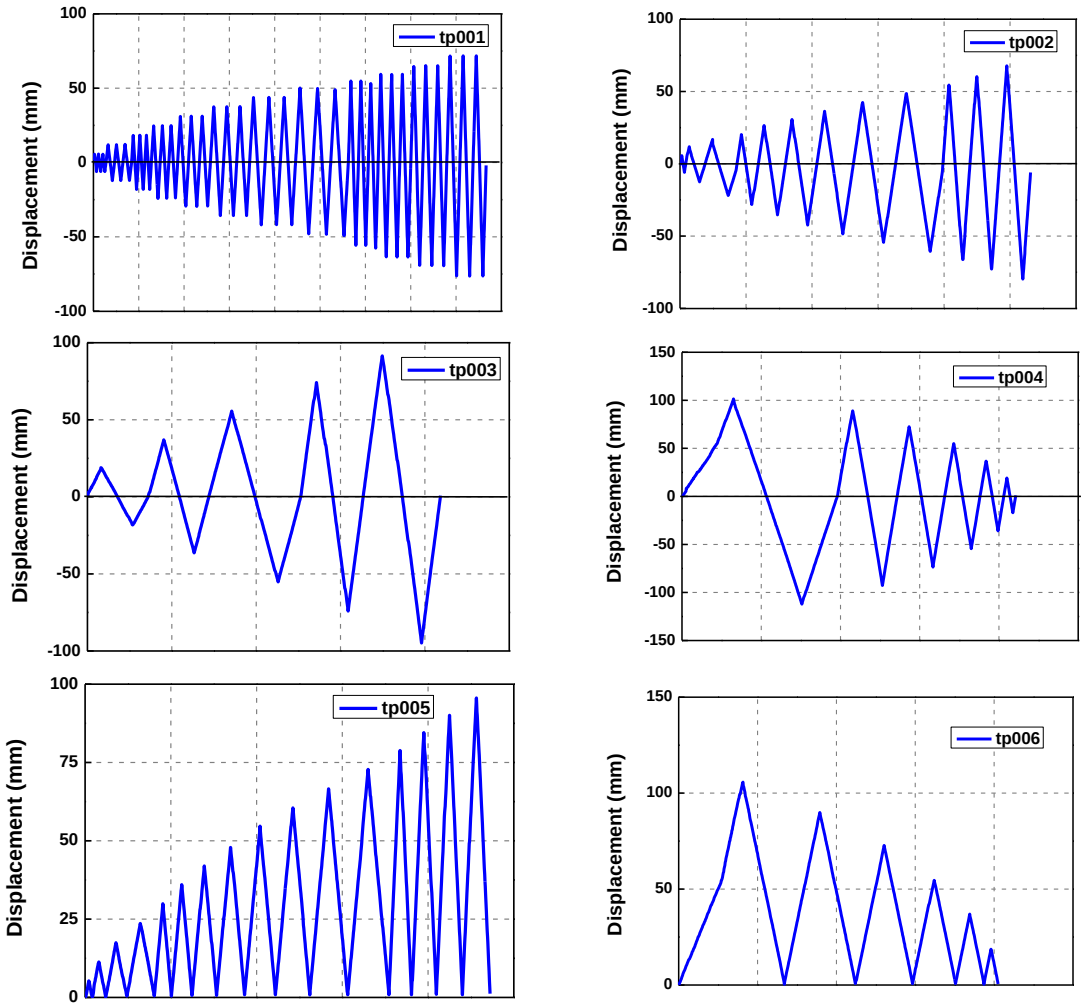

Fig. 2 Loading history for specimen tp001 to tp006

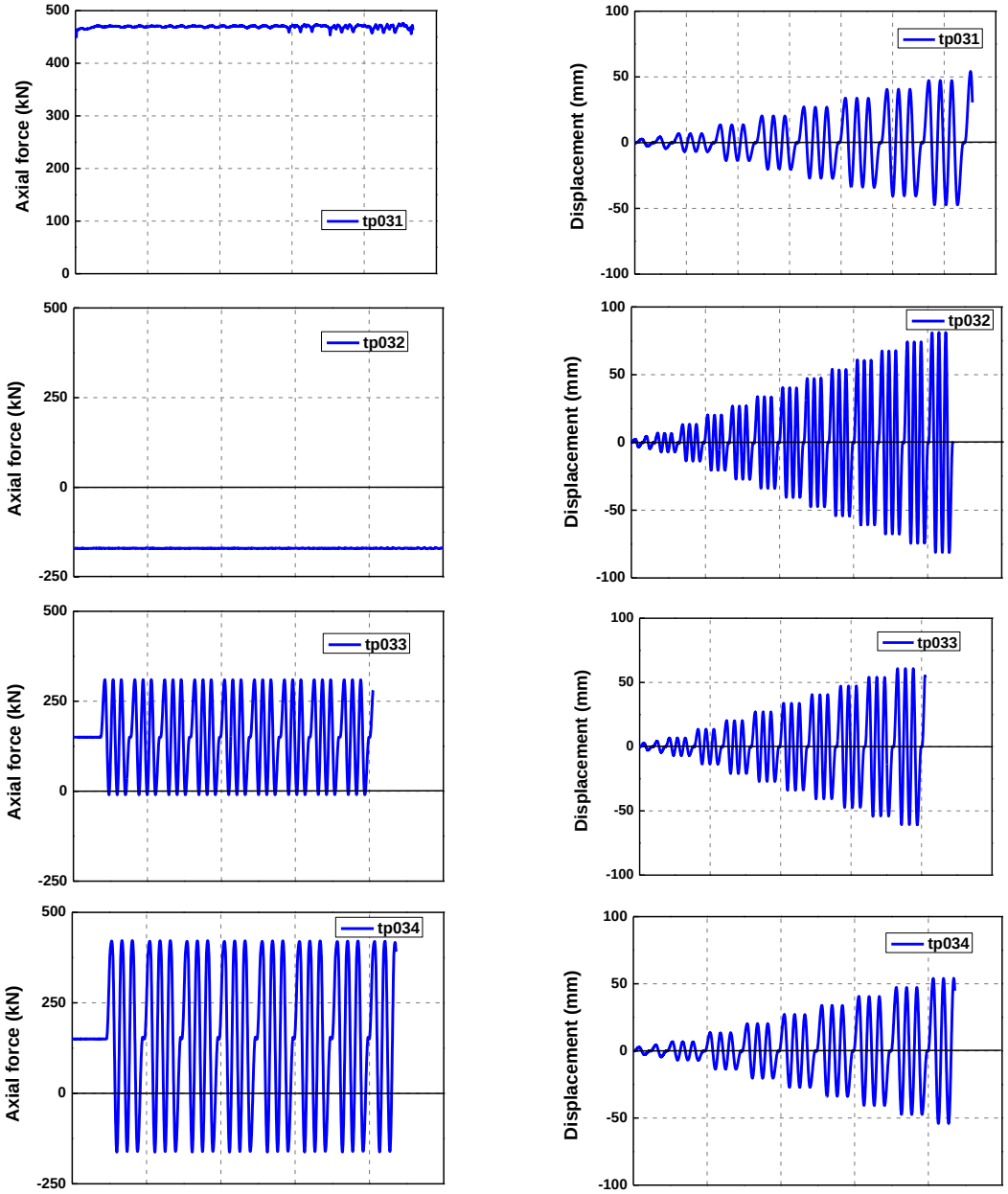

Fig. 3 Loading condition for specimen tp031 to tp034

constant tension axial load corresponding to -4.6 % of the normalized axial load; (tp033) varying axial load corresponding to -0.3% to 8.5% normalized axial load; and for (tp034) a varying axial load corresponding to -4.6% to 11.4% normalized axial load. The lateral displacement was stepwise increased such as 0.5%, 1%, 1.5% drift, until failure, with three load reversals cycles that were applied per step.

3. Test results

3.1 Effect of loading history

Fig. 4 shows the experimental hysteresis curves of the six specimens tp001 to tp006. Lateral force-displacement curves of specimen tp001 to tp003 show the effect of number of load cycles in

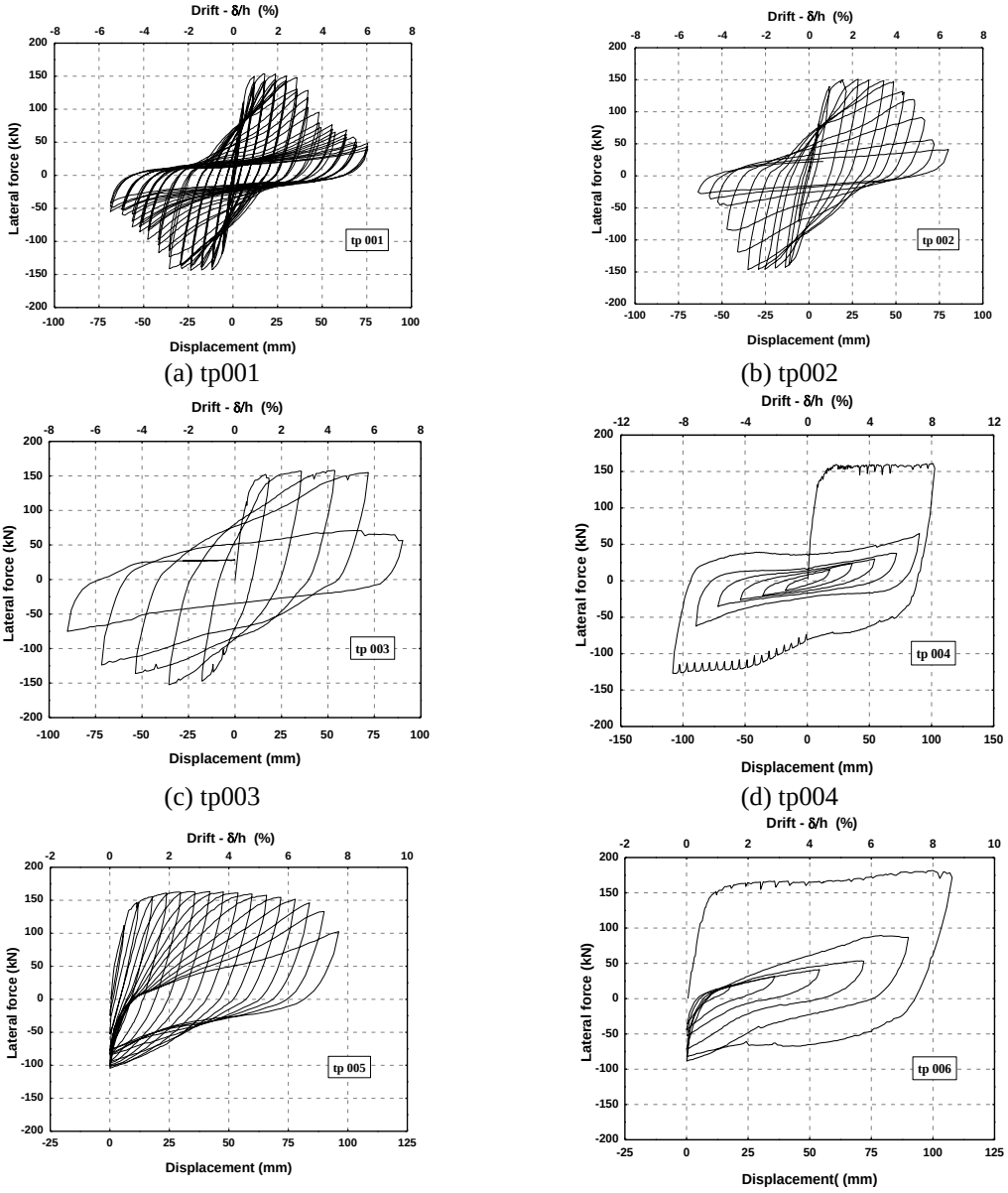

(a) tp001 (b) tp002

(c) tp003 (d) tp004

(e) tp005 (f) tp006

Fig. 4 Loading hysteresis for specimens tp001 to tp006

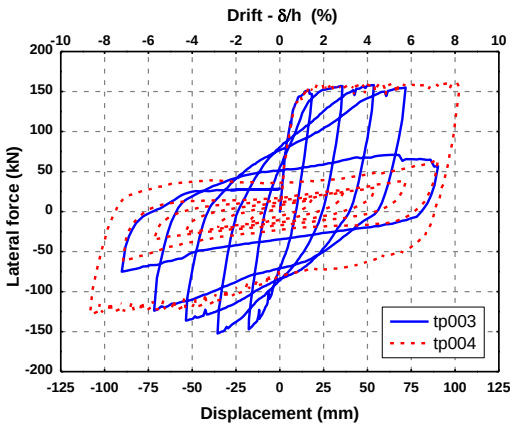

(a) tp003 and tp004

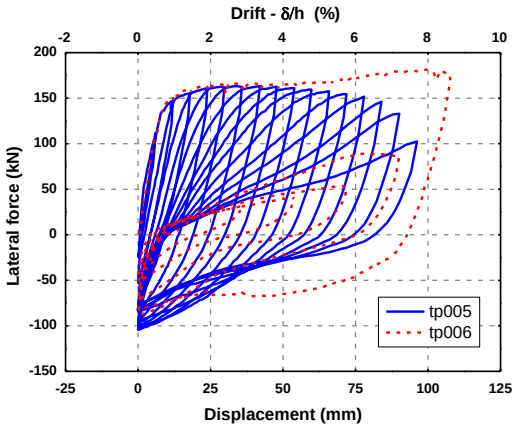

(b) tp005 and tp006

Fig. 5 Comparison between lateral forces vs. displacement

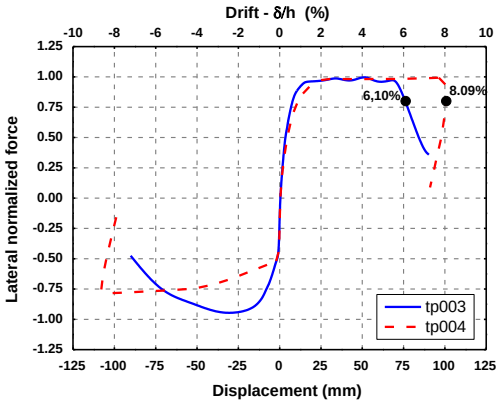

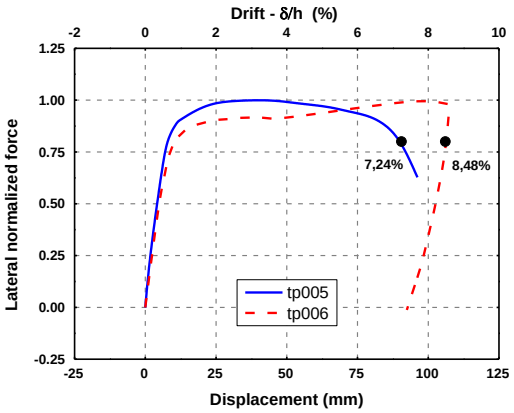

Fig. 6 Comparison between lateral normalized forces vs. displacement

the stepwise increasing loading. As the number of load step increases, the ultimate displacement decreases. Fig. 4(d) shows the lateral force vs. lateral displacement hysteresis for the stepwise decrease loading for specimen tp004. Compared to tp003, the restoring force on the first excursion toward $18\delta_y$ is stable until $18\delta_y$ (8.7% drift) under the stepwise decrease loading, while the restoring force of specimen tp003 under the stepwise increase starts to significantly deteriorate after $12\delta_y$. Fig. 4(e) and Fig. 4(f) show the relationship of the lateral force versus the lateral displacement of specimens tp005 and tp006 subjected to a loading only in one direction.

Fig. 5(a) shows a comparison between specimen tp003 and tp004. It is clearly shown that tp004 performed very well without strength degradation until a drift of 8%. The hysteresis loop shows a parallelogram shape, implying that energy dissipation capability is quite large. However, for specimen tp003, a significant drop in the lateral force was observed at less than 6% drift. The difference of the stepwise decrease and increase loadings was also apparent for specimens loaded in one direction as shown in Fig. 5(b) for specimens tp005 and tp006. Hysteresis loop of specimen

tp006 was stable from the beginning of first loading until a drift of more than 8% drift. However, at the second cycle the lateral force was only 88kN, showing around 45% drop in strength compared to the first cycle.

Fig. 6 shows the normalized envelope curves of specimens tp003-tp004 and tp005-tp006, respectively, on the same graph. The normalized force was defined as the ratio between the actual lateral forces to the maximum peak force. The black dots on the graphs correspond to the drift at 20% drop in strength. It is well seen that specimens tp004 and tp006, under stepwise decrease loading, have a larger drift angle at 20% drop than specimens tp003 and tp005. Besides that, a significant difference was observed in the negative loading side between the envelope curve of specimen tp003 and tp004. From this observation, we may say that the seismic performance of a structure or its components in general, depends on the loading history. In other words, the performance of structure depends on the input motion and its location to the earthquake source, near or far field earthquake.

3.2 Effect of axial load

The hysteresis curves of specimens tp031 to tp034 are illustrated in (Fig. 7). A quite symmetrical curve was obtained for specimen tp031 and tp032 under, respectively, a constant

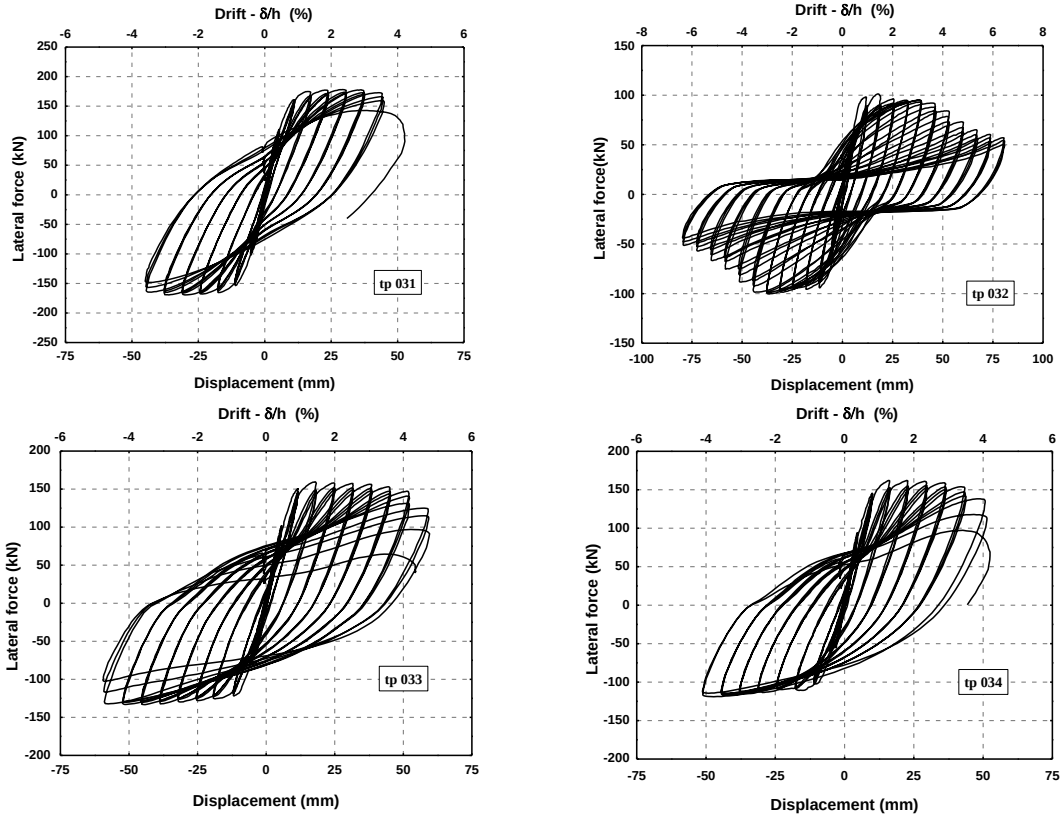

Fig. 7 Hysteresis loops of the lateral force vs. lateral displacement relations

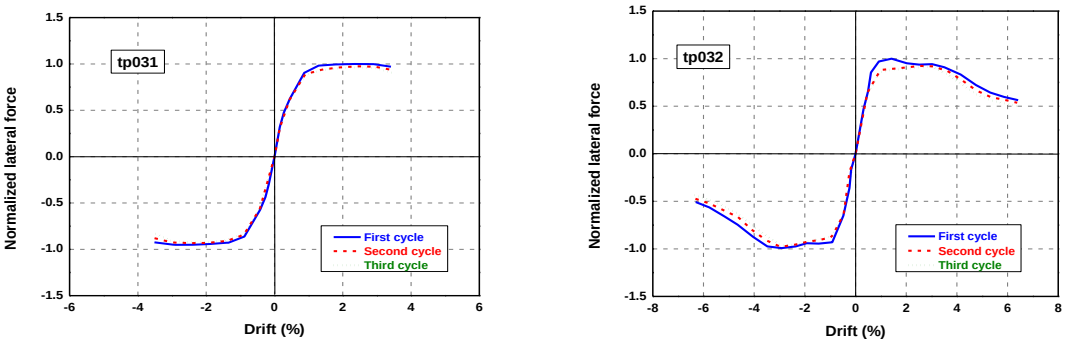

Fig. 8 Normalized load-drift relationships

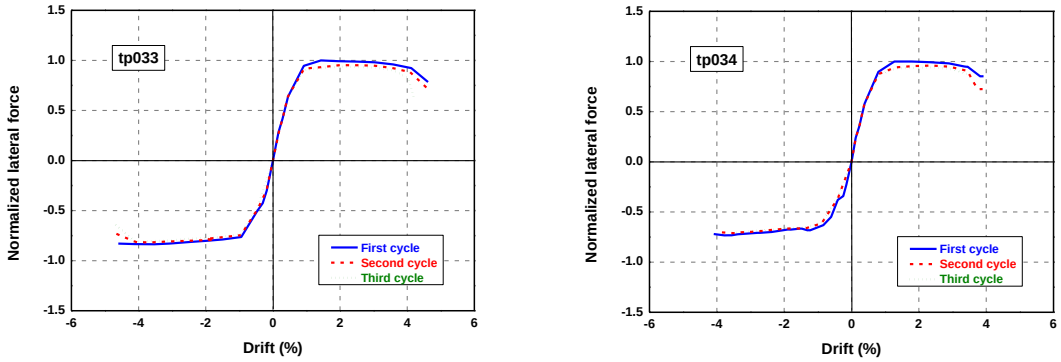

Fig. 8 Normalized load-drift relationships

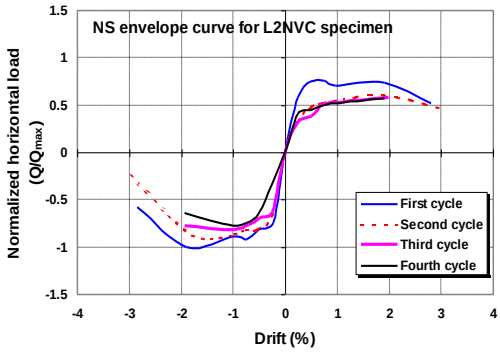

Fig. 9 Load-drift relationship L2NVC (Bechtoula *et al*. 2006)

compression and tension axial load. The maximum-recorded lateral force of specimen tp032 was only 55% of that recorded for specimen tp031. This result emphases the importance of concrete contribution to the overall performance of a specimen during a seismic event. It was reported (Sakai and Kawashima 2002) that for specimen tp032, the shear movement occurs along shear cracks, but did not result in a significant deterioration of lateral restoring force. The lateral restoring force starts to deteriorate at 3.5-4% drift when the cover concrete started to spall off. At 4.5% drift, the restoring force reduced to around 60% of the maximum values. The test was terminated at 6% drift after the cutoff of the longitudinal bar. At this stage, not only the cover

concrete but also the core concrete suffered extensively for nearly 40% of its total sectional area. Among 20 longitudinal bars, one ruptured and 19 bars buckled in complicated modes. Shear failure did not take place until the end of the test.

For specimens tp033 and tp034, the restoring forces were always larger in positive lateral displacement than negative lateral displacement. This was due to the increased compression vertical load in the positive lateral displacement. It can be also noted that deterioration of the restoring force is larger in the positive lateral displacement than the negative lateral displacement that was nearly unseen.

Effect of axial load intensity on the force-drift relationships was not clearly observed while comparing the envelope curves of the first, second and third envelops curves; as illustrated in Fig. 8. This is mainly due to the small intensity of the normalized axial load which was in the worst case only 12.8% for specimen tp031. The second co-author carried out a testing program (Bechtoula *et al*. 2006) where he found that the strength degradation is highly dependent on the axial load intensity. As an example Fig. 9 shows a test result of specimen L2NVC tested under a variable load varying with the maximum normalized axial load of 0.6. The specimen was loaded with four cycles at each prescribed drift. Under high axial load corresponding to the negative drift, a large drop in the normalized horizontal load was observed from the first-cycle to the fourth-cycle envelope curve. However, under a low axial load corresponding to the positive drift, difference was minimal between the second, third and fourth-cycle envelope curves

3.3 Energy dissipating and equivalent viscous damping variation

Variation of the equivalent viscous damping factor was computed using the first cycle loops at each of the imposed drift angle (Shibata and Sozen 1976). The equivalent viscous damping, H_{eq}, was computed using the following expression:

$$H_{eq} = \frac{1}{2\pi}\frac{\Delta W}{W} \tag{1}$$

In which ΔW is the energy dissipated during one reversed cycle and W is the elastic energy as defined in following (Fig. 10).

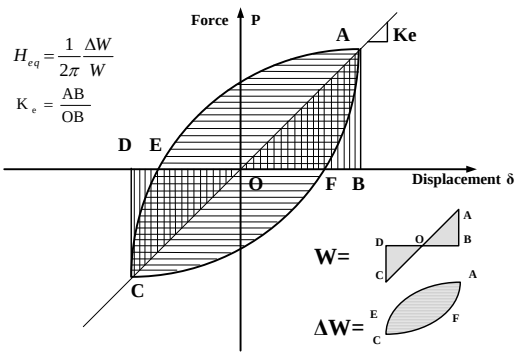

Fig. 10 Definition of the equivalent hysteretic damping ratio

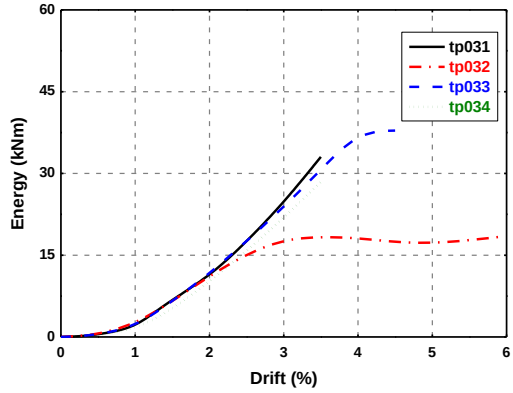

(a) Energy dissipation per cycle

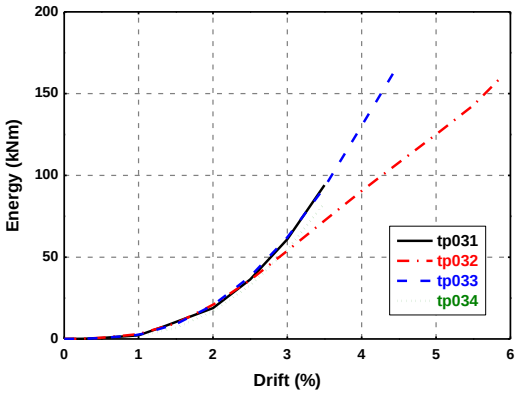

(b) Cumulative dissipated energy

Fig. 11 Energy dissipation

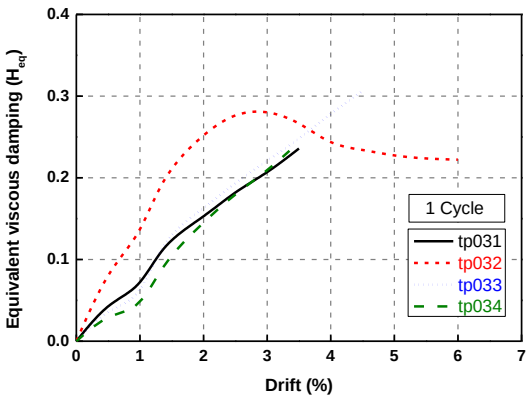

(a) Using the first cycle loop

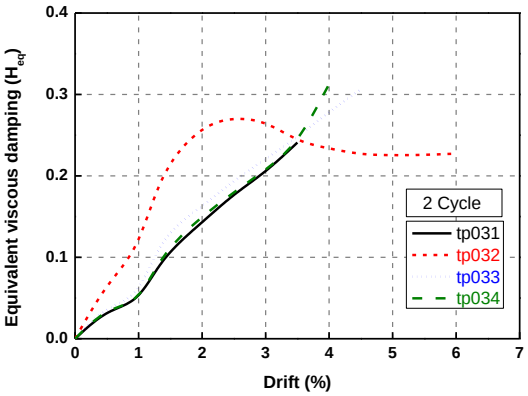

(b) Using the second cycle loop

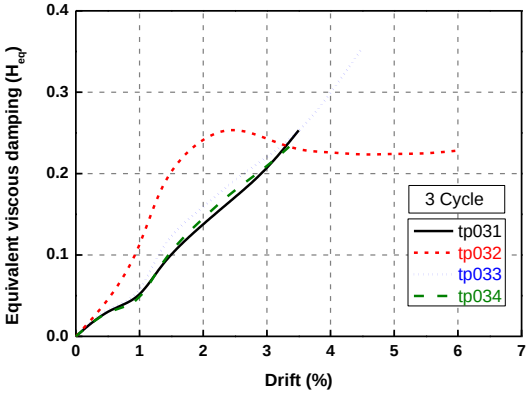

(c) Using the third cycle loop

Fig. 12 Comparison of the equivalent viscous damping variation

Fig. 11 shows the dissipated energy per cycle and the cumulative dissipated energy of specimen tp031 to tp034. It can be observed through Fig. 11(a) that the energy dissipated per cycle for

specimen tp032 is constant from 3% to 6% drift, which was not the case for the three other specimens. This is due mainly to the constant axial force that was applied to the specimen, tp032. The amount of energy dissipated per cycle was the same for the four specimens until a drift of 2%. Beyond that a bifurcation is observed, see Fig. 11(a). The cumulative dissipated energy is illustrated in Fig. 11(b). At 4.5% drift, the cumulative dissipated energy of specimen tp032 was only 65% of that of specimen tp033. Fig. 12 shows variation of the equivalent viscous damping, H_{eq} Specimens tp031, tp033 and tp034 showed the same variation until a drift of 3.5%., either using the first, second or the third cycle loop. For these specimens the H_{eq} increase gradually until the test end. However, for specimen tp032, the peak value of the equivalent viscous damping was observed around 2.5% drift for the three used cycles with a value of 0.27%. Beyond that, H_{eq} decreased and became constant after 4% drift with a value of 0.22%. Fig. 13 shows a comparison of the hysteresis loops of the four specimens (tp031, tp032, tp033 and tp034) at three 1.5%, 2.5% and 3.5% drift, respectively. Pinching of the hysteresis curve of specimen tp032 can be seen at 3.5% drift. Specimen tp032 and tp034 showed nearly the same trend of variation for the three compared drifts. Specimen tp031, under a constant compression axial load demonstrated a fat hysteresis loop at 3.5% drift, showing a very good energy dissipation capability.

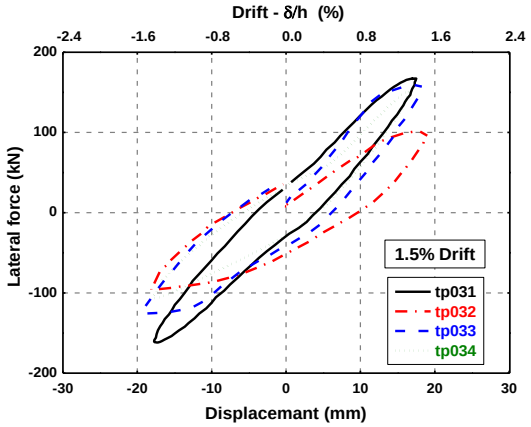

(a) At 1.5%

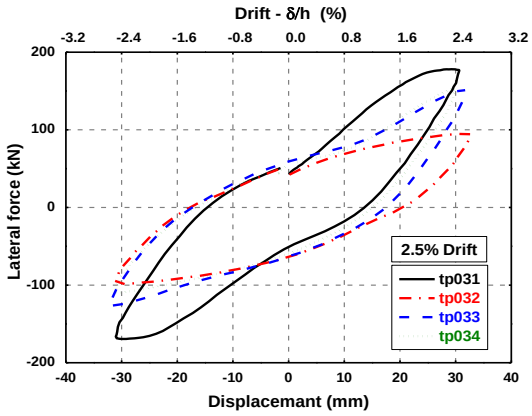

(b) At 2.5%

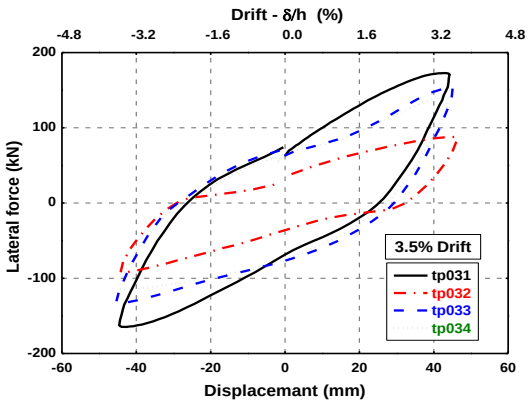

(c) At 3.5%

Fig. 13 Comparison of hysteresis loops at different drifts

3.4 Normalized equivalent stiffness and strength degradation

Variation of the normalized stiffness (k/k_0) with respect to the drift angle is illustrated in Fig.14; with (k) is the stiffness at a given drift and (k_0) denote the initial elastic stiffness. It appears that the stiffness degradation curve has the same shape for the four specimens. At k/k_0 = 0.25, the corresponding drifts were 2.5, 2.8, 3.15 and 3.5 for tp031, tp032, tp034 and tp033, respectively.

Fig. 15 shows the decay in term of horizontal load carrying capacity of the four specimens. Until 4 cycles, no big difference was observed between the specimens. However, beyond that limit, strength degradation was more pronounced for specimen tp034 than the others. As an example, at 5 cycles, the ratios (Q/Q_p) of the strength at a given drift, Q, to the peak strength, Q_p, were, respectively, 0.42, 0.57, 0.54 and 0.68 specimen tp034, tp033, tp032 and tp031.

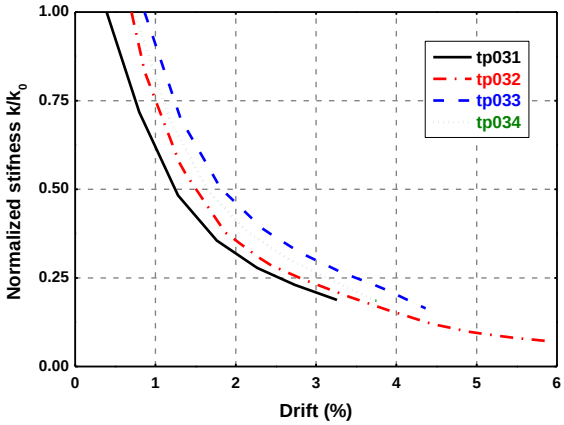

Fig. 14 Variation of the normalized stiffness

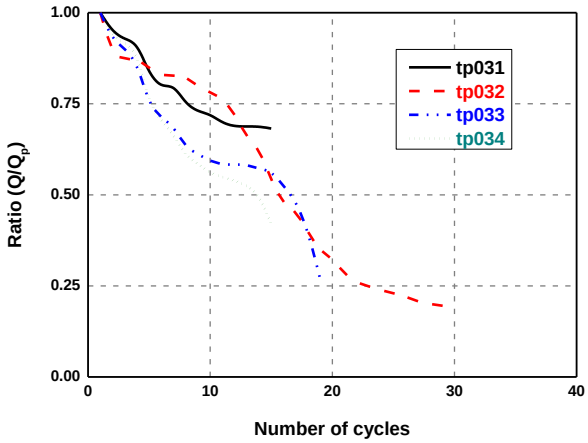

Fig. 15 Normalized strength degradation with respect to the number of cycles

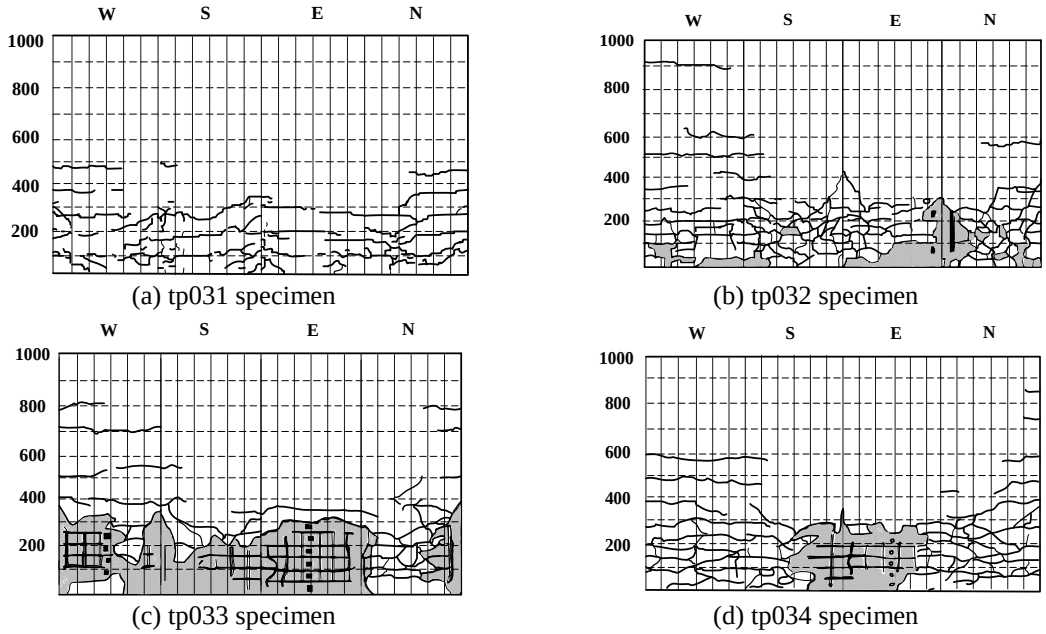

(a) tp031 specimen (b) tp032 specimen

(c) tp033 specimen (d) tp034 specimen

Fig. 16 Observed damage at test end

Fig. 16 shows the observed damage at test end of the four specimens. The piers were laterally loaded in West-East direction. It is noted that the axial load in compression increases when the pier is laterally loaded toward East direction, and the axial load in compression decreases (the smallest axial stress of concrete is 0 in tp033 and -1MPa in tp034) when the pier is laterally loaded toward West direction.

The failure of tp031 specimen progressed from spalling off covering concrete and outward buckling and rupture of longitudinal bars. In the tp033 and tp034 specimens, compression failure of concrete in the plastic hinge is always larger at East side than West side, since the flexural compression and the compression due to the vertical load combined resulting in larger compression in the East side than the West.

4. Numerical modeling

4.1 Materials and elements models

Numerical models for the tested specimens were developed and analyzed using SeismoStruct software (SeismoStruct 2012). The SeismoStruct is a finite element package capable of predicting the large displacements behaviour of space frames under static or dynamic loading, taking into account geometric nonlinearities and material inelasticity. Several models are available for concrete and steel materials as well as for the frame elements. With regard to the material models, the concrete and the steel reinforcement models available in SeismoStruct were used. The concrete model is a uniaxial nonlinear constant confinement model that follows the constitutive relationship

proposed by Mander *et al*. (1988).

The confined and unconfined concrete is modelled using a unified stress-strain model based on the formulation initially proposed by Mander *et al*. see Fig. 17(a), for a concrete subjected to uniaxial compressive loading and confined by transverse reinforcement. The strain at peak stress was taken as ε_c = 0.002 mm/mm; the confinement factor was assumed as 1.2 for confined concrete and 1 for the unconfined concrete. The steel model is based on the stress-strain relationship proposed by Menegotto and Pinto (1973); see Fig. 17(b), coupled with the isotropic hardening rules proposed by Filippou *et al*. (1983). Regarding the other model parameters, the default values indicated by SeismoStruct were adopted, except for R_0, which was made equal to 19.5 instead of 20.0 (default value). This parameter controls the shape of the transition curve between initial and post-yield stiffness, the indication of all the other parameters results common for both: modulus of elasticity E_s = 200 GPa, strain hardening parameter μ=0.005. The formulation of the element determines whether the element based on displacement shape functions (stiffness or displacement-based element) or interpolation function for forces (flexibility or force-based element). The consideration of the element type is important since it controls the distribution of the inelastic strains. Therefore, the outcome of the analysis will strongly depend on the chosen element formulation, the number and position of integration points along the element length.

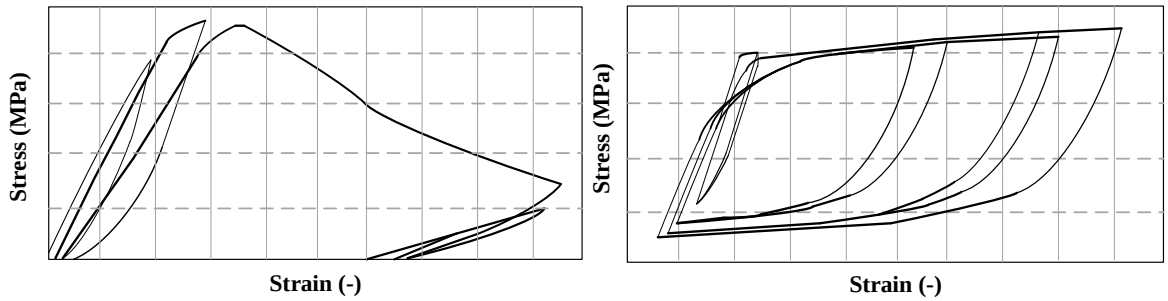

(a) Nonlinear constant confinement concrete model (b) Menegotto-pinto steel model

Fig. 17 Stress-Strain model for the structural materials adopted in SeismoStruct

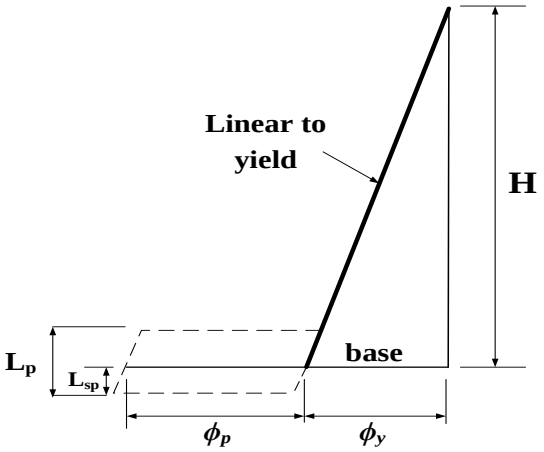

Fig. 18 Idealization of curvature distribution

The distributed inelasticity frame elements were implemented with the displacement-based (DB) finite elements formulations. In this case, cubic hermitian polynomials are used as displacement shape functions, corresponding for instance to a linear variation of curvature along the entire element's length. Since the curvature field can be highly nonlinear during inelastic analysis such as pushover or inelastic dynamic time history, a refined discretization (meshing) of the structural element (typically 4-5 elements per structural member) is required with a DB formulation.

The 1.35 m high pier was built with inelastic frame elements with displacement-based (infrmDB element) modeled by four finite elements. The first two elements, from the bottom, were subdivided into 6 sub-elements. The two upper remaining elements were subdivided into 3 sub-elements. Two integration sections per element were used (Gauss quadrature), each one containing around 250 integration points. The pier was modeled with the length of the plastic hinge L_p over which strain and curvature are considered equal to the maximum value at the base pier. The plastic hinge length incorporates the strain penetration length L_{sp} as shown in (Fig. 18). Further, the curvature distribution higher up the pier assumed linear, in accordance with the SDOF model. The strain penetration length, L_{sp}, was taken as:

$$L_{sp} = 0.022 f_{ye} d_{bl} \tag{2}$$

where f_{ye} and d_{bl} are the expected yield strength and diameter of the longitudinal reinforcement.

4.2 Experimental and numerical comparison

Fig. 19 shows a comparison between the experimental and the analytical results in terms of hysteresis loops, lateral force-displacement, or drift, for the tested specimens. As illustrated in the figure, the analytical results show reasonable agreement with the experimental ones. The analysis not only correctly predicted the stiffness, load, and deformation at the peak, but also captured the post-peak softening as well.

The constructed models for specimen tp033 and tp034 captured the effect of the axial load variation on the piers performance. The results show that the compressive axial load in the push direction increased the strength capacity, and that the tensile axial load in the pull direction reduced the strength capacity.

The maximum experimental and analytical horizontal peak loads of the four specimens are summarized in Table 2. In all cases the ratio experimental peak strength to the analytical one (Q_{exp}/Q_{ana}) was greater than 0.95 except for specimen tp032 in negative side. The mean ratios of experimental-to-analytical maximum peaks were 0.96 with a coefficient of variance (COV) of 1% for the positive side and 0.97 with a coefficient of variance (COV) of 4% for the negative side.

Maximum peak strengths were also assessed using the:

- ACI code
- ACI equivalent stress block, ACI (SB)
- Eurocode

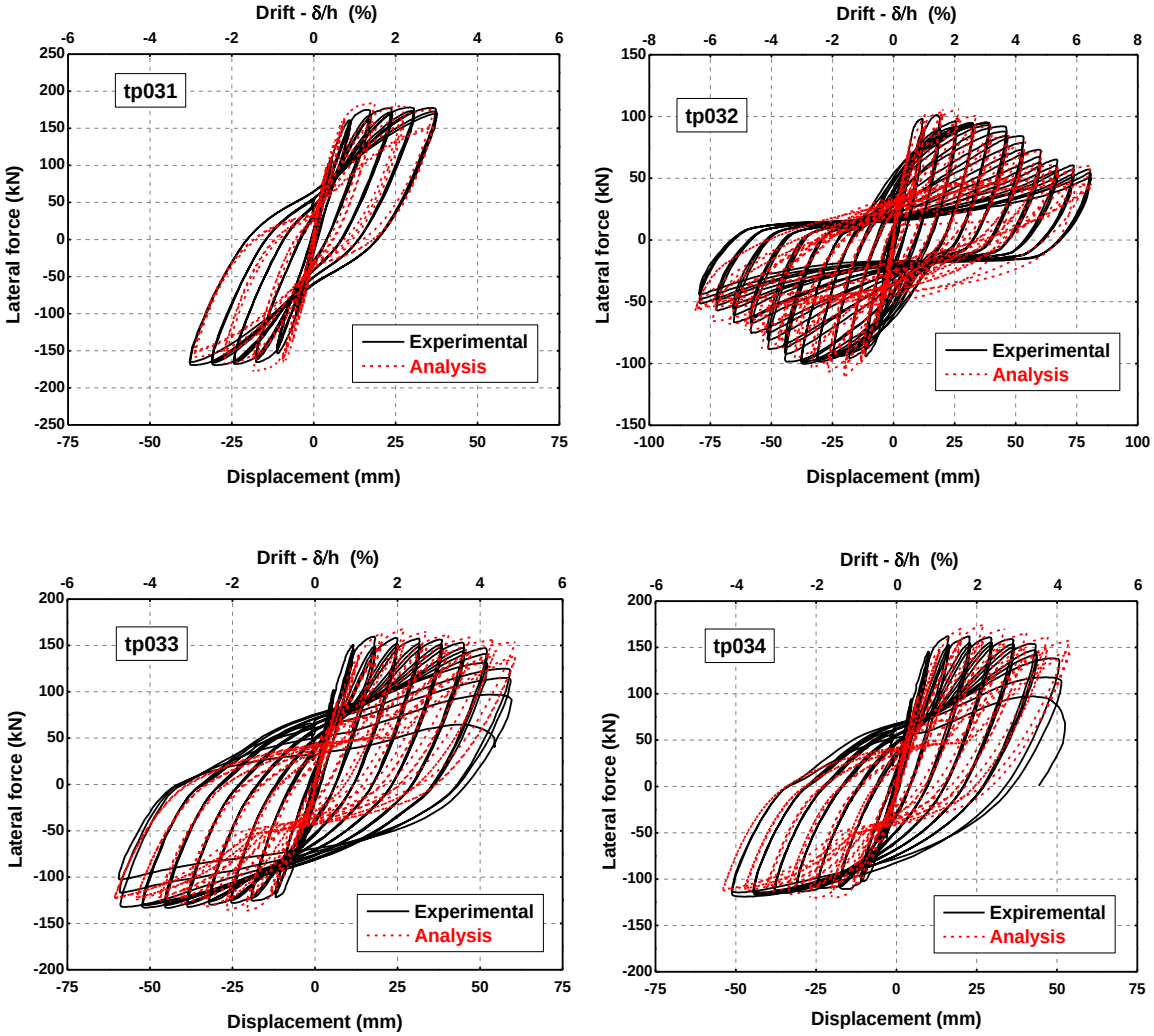

Fig. 19 Hysteresis loops of the lateral force vs. lateral displacement relations

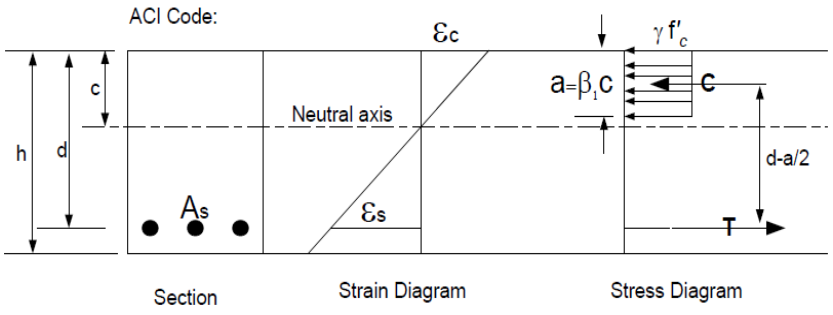

Fig. 20 Strain distribution and stress block in ACI code

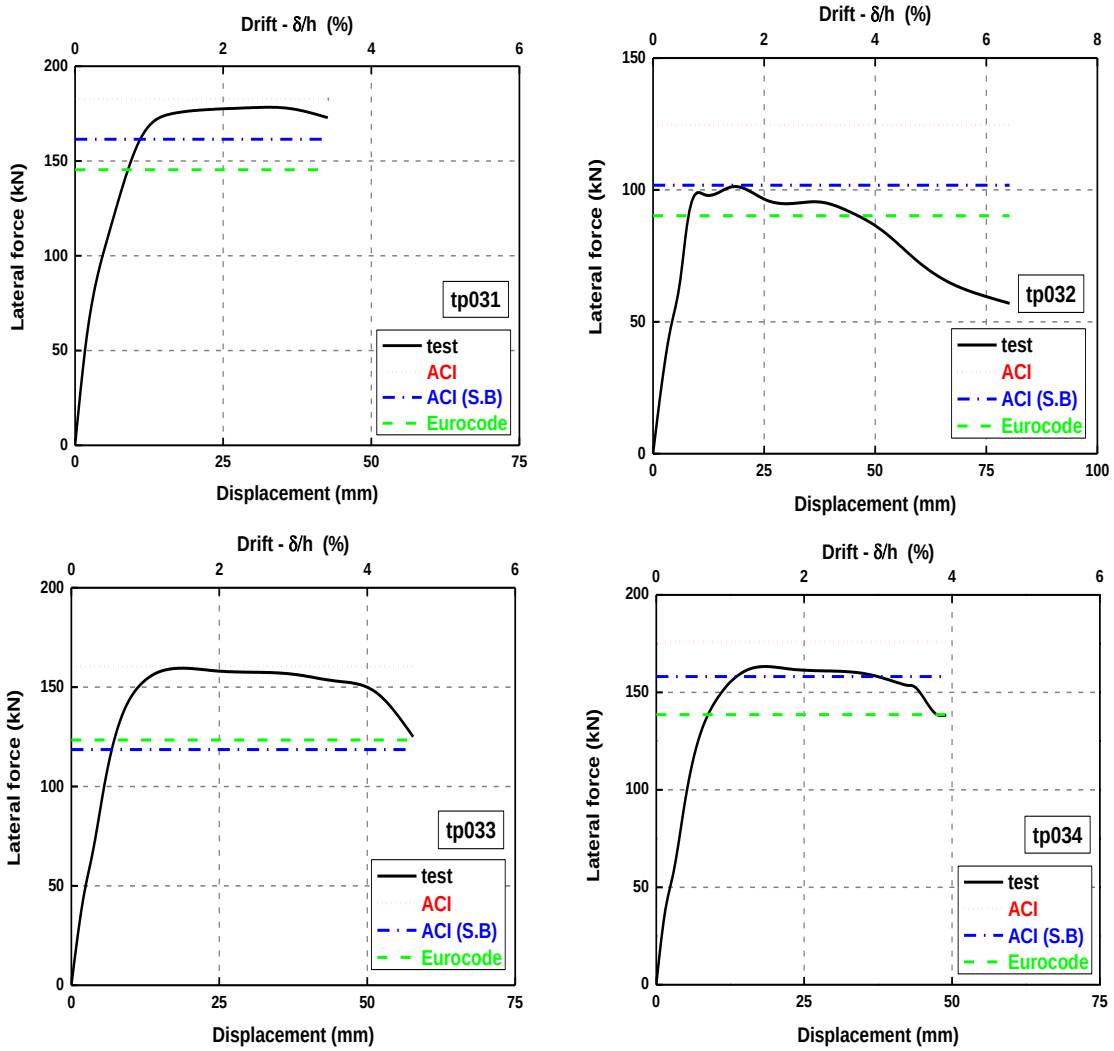

Fig. 21 Comparison of experimental result and predicted shear strength

Table 2 Comparison between the experiment and the analytical peak strengths

Specimen	Positive side			Negative side		
	Experiment	Analysis	Ratio	Experiment	Analysis	Ratio
	Q_{exp} (kN)	Q_{ana} (kN)	(Q_{exp}/Q_{ana})	Q_{exp} (kN)	Q_{ana} (kN)	(Q_{exp}/Q_{ana})
tp031	178.1	184.3	0.97	-169.4	-178.1	0.95
tp032	101.2	106.2	0.95	-100.4	-110.9	0.91
tp033	159.5	168.1	0.95	-133.3	-136.4	0.98
tp034	162.1	170.9	0.95	-119.0	-116.5	1.02
Mean			0.96			0.97
COV			0.01			0.04

Table 3 Comparison between the experiment, ACI, ACI stress block and the Eurocode

		Lateral load (kN)				Ratios		
Specimen	P (kN)	V_{test}	$V_{ACI(Eq)}$	$V_{ACI(SB)}$	$V_{Eurocode}$	$V_{ACI(Eq)}/V_{test}$	$V_{ACI(SB)}/V_{test}$	$V_{Eurocode}/V_{test}$
tp031	470	178.1	182.6	161.5	145.4	1.03	0.91	0.82
tp032	-170	101.2	124.6	101.8	90.2	1.23	1.01	0.89
tp033	310	159.5	160.4	118.6	123.4	1.01	0.74	0.77
	-10	133.2	111.9	149.2	79.5	0.84	1.12	0.60
tp034	420	162.1	175.9	158.1	138.6	1.08	0.98	0.85
	-170	119.0	124.6	101.8	90.2	1.05	0.86	0.76
Mean						1.04	0.93	0.78
COV						0.013	0.014	0.008

According to ACI 318-11(ACI 2011), the nominal shear strength is computed by:

$$V_n = V_c + V_s \tag{3}$$

where V_c and V_s are the nominal shear strength provided by concrete and shear reinforcement, respectively.

For members subjected to axial compression V_c is given by:

$$V_c = 2\left(1+\frac{P}{2000A_g}\right)\sqrt{f'_c}bd \tag{4}$$

And for members subjected to significant axial tension, shear strength provided by concrete is assessed as follow:

$$V_c = 2\left(1+\frac{P}{500A_g}\right)\sqrt{f'_c}bd \tag{5}$$

where P is axial load subjected to the column; A_g is gross cross-sectional area of the column; f'_c is concrete compressive strength; and b is the width of column; and d is the effective depth of column. The transverse reinforcement contribution is calculated as:

$$V_s = \frac{A_v f_y d}{s} \tag{6}$$

where A_v is the area of transverse reinforcement within the spacing s, and f_y is the yield stress of hoops or spirals.

The same expression of V_s is given by the EC2 (Eurocode 2004). For the shear strength

provided by concrete V_c, the EC2 proposes the following equation:

$$V_c = [\tau_{rd} k(1.2 + 40\rho_l) + 0.15\sigma_{cp}]bd \tag{7}$$

where τ_{rd} the stress due to the axial force is, ρ_l is the ratio of longitudinal reinforcement.

The equivalent stress block proposed by the ACI code, shown in Fig. 20, was used to evaluate the peak loads and compared to the experimental test results.

Fig. 21 shows the experimental lateral force-displacement envelope curves and the predicted shear capacities using the ACI, ACI stress block and the EC2. Comparisons between the experimental and the predicted lateral peak forces are summarized in Table 3. It is clearly shown that the Eurocode underestimated the real capacity of all specimens. The prediction using the ACI Eq. (3) and the ACI stress block gave very good results that were the closest to the experimental ones, with an average of 1.04 and 0.93, respectively.

5. Damage and fragility curves

5.1 Damage progress

The damage for individual elements is calculated based on element data such as element deformations, forces, or dissipated energy. These engineering parameters must be extracted from the solution and processed for calculating a damage index, DI. A damage model is defined as an operator that calculates the damage index by applying a specific damage rule.

The damage index can be recorded for subsequent loss assessment and in some cases; it may be used by the analysis components for degrading constitutive stiffness or strength parameters.

The combined damage model introduced by Park and Ang (1985) is widely used due to its simplicity and the fact that calibration information is available. Park-Ang is a combined damage model, which was originally calculated for RC components. The Park-Ang model calculates the damage index is a linear combination of the damage caused by excessive deformation, and repeated cyclic loading, captured in the form of dissipated energy. The general form of the Park-Ang damage formulation is as follows:

$$\mathrm{DI} = \frac{\delta_{\max}}{\delta_{\mathrm{u}}} + \beta \frac{\int \mathrm{dE}}{\mathrm{F_y}.\delta_{\mathrm{u}}} \tag{8}$$

where $\delta_{\max}$ is the maximum displacement of the structural member, δ_u is the ultimate displacement, $\int$dE is the dissipated hysteretic energy and F_y is the yielding strength of the structural member; β is a degradation parameter which represents the influence of cyclic response on column damage and can be estimated with empirical expressions based on structural parameters.

A detailed classification of damage levels suggested by Park *et al*. (1985) is used to relate the observed empirical damages and the calculated damage indices.

The computed damage to all specimens using Park and Ang models described above is shown in Fig. 22. For all specimens, Park and Ang model shows little or no damage through the first ten cycles. Gradual damage progression throughout the load history was assessed for each specimen. Park and Ang model provided a very good measure of damage at different limit states.

For specimen tp032 with constant tension axial load was subjected to much larger drift amplitude. Failure of the specimen was recorded in less than 30 cycles. The Park-Ang model seems to perform better when the displacement amplitudes are significantly larger than the yield displacement.

Table 4 Park-Ang damage level classifications

Damage level	Damage index	Damage measure
I	DI < 0.1	No damage, localized minor cracking
II	0.1 ≤ DI ≤ 0.25	Minor damage, light cracking throughout
III	0.25 ≤ DI ≤ 0.4	Moderate damage, severe cracking, localized spalling
IV	0.4 ≤ DI ≤ 1.0	Severe damage, crushing of cracking, reinforcement exposed
V	DI ≥ 1	Loss of element load resistance

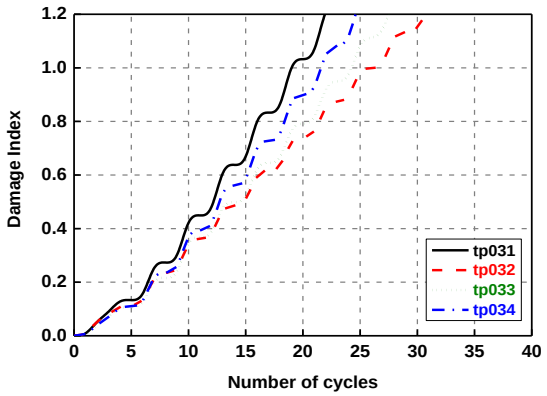

Fig. 22 Progressive Damage for all specimens

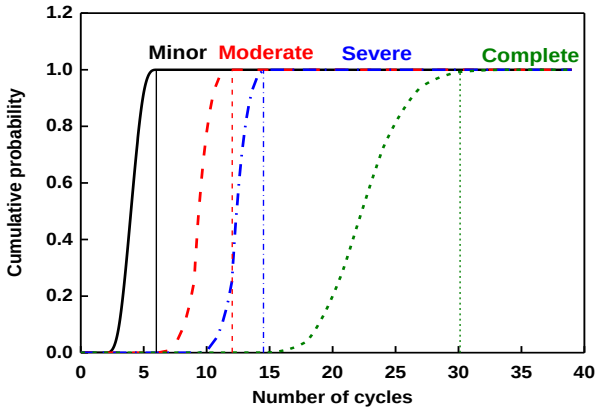

Fig. 23 Fragility curves for four reinforced concrete bridge piers

5.2 Fragility curves

Fragility curves express the probability of structural damage due to cyclic loading as a function of number of cycles. Based on the computed Park and Ang damage index shown above for the four tested specimens, a set of fragility curves for the bridge piers were constructed assuming a lognormal distribution.

Fragility curves indicate the probability of reaching or exceeding a previously defined damage state. As previously mentioned, five damage states were used (see Table 4); these are no damage, slight, moderate, extensive and complete damage. Fig. 22 shows the damage states and its corresponding damage index.

Once the damage index value is obtained at each cycle, the damage state is classified using Table 4. The cumulative probability distribution for each damage state for the four specimens was assessed and a plot was created. A lognormal curve was fitted to develop a relationship between number of cycles and damage index by using least squares approach. In order to obtain the two parameters that define the lognormal distribution, the Microsoft Excel Solver Tool was used.

Fig. 23 shows the fragility curves for four reinforced concrete bridge piers. It can be shown that until 6 cycles no difference in damage distribution is observed for the four specimens. Using the Park and Ang damage classification given in Table 4, it was concluded that: for no damage level the number of cycles is between (0~6) cycles; minor damage level is between (6~12) cycles; moderate damage level is between (12~14); severe damage level is between (15~30) cycles and for complete damage level is over 30 cycles.

6. Conclusions

In this paper some results of an analytical research program conducted to assess the seismic behavior of reinforced concrete bridge piers was presented. The analyzed specimens were chosen from the data bank of Professor Kazuhiko Kawashima. Effect of loading history and axial load intensity were considered in this analysis. All specimens, in total 10, had a square cross section of 400×400mm.

It was shown that the difference of the stepwise decrease and increase loadings was apparent for specimen's cyclically reversed (positive and negative sides) or loaded only in one direction (positive side). Stepwise decrease loaded specimens showed a larger drift angle at 20% strength drop. This shows clearly that the seismic performance of a structure or its components in general, depends on the loading history. In other words, the performance of structure depends on the input motion and its location to the earthquake source, near or far field earthquake. The dissipated energy for specimen tp032, under a constant axial load, was constant from 3% to 6% drift, which was not the case for the three other specimens. However, at 4.5% drift, the cumulative dissipated energy of specimen tp032 was only 65% of that of specimen tp033.

It appears that the stiffness degradation curve has the same shape for the four specimens. At $k/k_0 = 0.25$, the corresponding drifts were 2.5, 2.8, 3.15 and 3.5 for tp031, tp032, tp034 and tp033, respectively. Strength degradation was more important for specimen tp034 than the others. As an example, at 15 cycles, the ratios Q/Q_p were, respectively, 0.42, 0.57, 0.54 and 0.68 for specimen tp034, tp033, tp032 and tp031.

For specimens tp033 and tp034, compression failure of concrete in the plastic hinge was always

larger at East side than West side, since the flexural compression and the compression due to the vertical load combined resulting in larger compression in the East side than the West.

Numerical models for the tested specimens were developed and analyzed using SeismoStruct software. The analytical results show reasonable agreement with the experimental ones. The analysis did not only predicted the stiffness, load, and deformation at the peak with a good accuracy, but also captured the post-peak softening as well. In all cases, the ratio (Q_{exp}/Q_{ana}) was greater than 0.95 except for specimen tp032 in negative side where this value was 0.91. The mean ratios of experimental-to-analytical maximum peaks were 0.96 with a coefficient of variance (COV) of 1% for the positive side and 0.97 with a coefficient of variance (COV) of 4% for the negative side.

It was shown that the Eurocode underestimated the real lateral force capacity of all specimens. In general results found by the ACI Eq. (3) and the ACI stress block gave very good results that were the closest to the experimental ones, with an average of 1.04 and 0.93, respectively. This value was only 0.78 using the Eurocode.

Damage was assessed for the four specimens using Park and Ang damage index. It was observed that Park-Ang model performs better when the displacement amplitudes are significantly larger than the yield displacement. Based on the computed Park and Ang damage indices, a set of fragility curves for the four bridge piers were constructed assuming a lognormal distribution. Based on the adopted classification, it was concluded that: for no damage level the number of cycles is between (0~6) cycles; minor damage level is between (6~12) cycles; moderate damage level is between (12~14); severe damage level is between (15~30) cycles and for complete damage level is over 30 cycles.

Acknowledgements

This research was supported by the National Earthquake Engineering Research Center, CGS, Algeria. The authors wish to express their gratitude and thanks to Prof. Kazuhiko Kawashima, Japan, for sharing his experimental data bank.

References

ACI (2011), *Building Code Requirements for Structural Concrete and Commentary*, ACI 318-11, American Concrete Institute, Detroit.

Acun, B. (2010), "Energy based seismic performance assessment of reinforced concrete columns", Ph.D. Thesis, Middle East technical University, Ankara.

Acun, B. and Sucuoglu, H. (2012), "Energy dissipation capacity of reinforced concrete columns under cyclic displacements", *ACI Struct. J.*, **109** (4), 531-540.

Á lvarez, J.J., Aparicio, A.C., Jara, J.M. and Jara, M. (2012), "Seismic assessment of a long-span arch bridge considering the variation in axial forces induced by earthquakes", *Eng. Struct.*, **34**, 69-80.

Bae, S. and Bayrak, O. (2008), "Seismic performance of full-scale reinforced concrete columns", *ACI Struct. J.*, **105** (2), 123-133.

Bechtoula, H., Kono, S. and Watanabe, F. (2005), "Experimental and analytical investigations of seismic performance of cantilever reinforced concrete columns under varying transverse and axial loads", *J. Asian Architect. Build. Eng.*, **4**(2), 467-474.

Bechtoula, H., Sakashita, M., Kono, S., Fumio, W. (2006), "Seismic design proposal based on a study on RC

columns and frame sub-assemblage", *Fédération Internationale du Béton*, Proceedings of the 2nd International Congress, ID 9-31, Naples, Italy.
Chang, S.Y. (2010), "Experimental studies of reinforced concrete bridge columns under axial load plus biaxial bending", *J. Struct. Eng. ASCE*, **136**(1), 12–25.
Chen, Y., Feng, M.Q. and Soyoz, S. (2008), "large-scale shake table test verification of bridge condition assessment methods", *J. Struct. Eng.*, **7**, 1235-1245.
Cheok, G.S. and Stone, W.C. (1990), "Behavior of 1/6-Scale model bridge columns subjected to inelastic cyclic loading", *ACI Struct. J.*, **87**(6), 630-638.
El-Bahy, A., Kunnath, S.K., Stone, W.C. and Taylor, A.W. (1999a), "Cumulative seismic damage of circular bridge columns: benchmark and low-cycle fatigue tests", *ACI Struct. J.*, **96** (4), 633-643.
El-Bahy, A., Kunnath, S.K., Stone, W.C. and Taylor, A.W. (1999b), "Cumulative Seismic Damage of Circular Bridge Columns: Variable Amplitude Tests", *ACI Struct. J.*, **96**(5), 711-719.
Eurocode 2 (2004), *Design of Concrete Structures Part 1*, European Standard ENV 1992-1-1, Brussels.
Filippou, F.C., Popov, E.P. and Bertero, V.V. (1983), *Effects of Bond Deterioration on Hysteretic Behavior of Reinforced Concrete Joints*, Report EERC 83-19, Earthquake Engineering Research Center, University of California, Berkeley.
Fujikura, S., Kawashima, K., Shoji, G., Zhang, J. and Takemura, H. (2000), "Effect of the interlocking ties and cross ties on the dynamic strength and ductility of rectangular reinforced concrete bridge columns", *J. Struct. Mech. Earthq. Eng.*, **640**(I-50), 71-88.
Galal, K.E. and Ghobarah, A. (2003), "Flexural and shear hysteretic behaviour of reinforced concrete columns with variable axial load", *Eng. Struct.*, **25**, 1353-1367.
Han, Q., Du, X., Zhou, Y. and Lee, G. (2013), "Experimental study of hollow rectangular bridge column performance under vertical and cyclically bilateral loads", E*arthq. Eng. Eng. Vib.*, **12**(3), 433-445.
Iranmanesh, A. and Ansari, F. (2013), "An energy based damage assessment methodology for structural health monitoring of modern reinforced concrete bridge columns", *J. Bridge Eng.*, 10.1061/ (ASCE) BE.1943-5592.0000569.
Kawashima, K., Shoji, G. and Sakakibara, Y. (2000), "A Cyclic Loading Test for Clarifying the Plastic Hinge Length of Reinforced Concrete Piers", *J. Struct. Eng.*, **46**A, 767-776.
Mander, J.B., Priestley M.J.N. and Park, R. (1988), "Theoretical stress-strain model for confined concrete", *J. Struct. Eng.ASCE*, **114**(8), 1804-1826.
Menegotto, M. and Pinto, P. (1973), "Method of analysis for cyclically loaded reinforced concrete plane Frames Including Changes In Geometry And Non-Elastic Behavior Of Elements Under Combined Normal Force And Bending", *Proceedings of the IABSE Symposium on Resistance and Ultimate Deformability of Structures Acted on by Well Defined Repeated Loads*, Lisbon, 15-22.
Mullapudi, T. and Ayoub, A. (2013), "Analysis of reinforced concrete columns subjected to combined axial, flexure, shear, and torsional loads", *J. Struct. Eng.*, **139**(4), 561-573.
Park, Y.J. and Ang, A.H.S. (1985), "Mechanistic seismic damage model for reinforced concrete", *J. Struct. Eng. ASCE*, **111**(4), 722-739.
Park, Y.J., Ang, A.H.S. and Wen, K. (1985), "Seismic damage analysis of reinforced concrete buildings", *J. Struct. Eng. ASCE*, **111**(4), 740-757.
Sakai, J. and Kawashima, K. (2002), "Effect of varying axial loads including a constant tension on seismic performance of reinforced concrete bridge piers", *J. Struct. Eng. JSCE*, **48**A, 735-746.
Salawu, O.S. and Williams, C. (1993), "Review of full-scale dynamic testing of bridge columns", *Eng. Struct.*, **17** (2), 113-121.
Seismo Struct, (2012), "A computer program for processing strong motion data", Seismosoft Ltd, website: www.seismosoft.com.
Sezen, H. and Moehle, J.P. (2006), "Seismic tests of concrete columns with light transverse reinforcement", *ACI Struct. J.*, **103**(6), 842-849.

Sheikh, S.A. (1978), "Effectiveness of rectangular ties as confinement", Ph.D. Dissertation, University of Toronto, Toronto.

Sheikh, S.A. and Toklucu, M.T. (1993), "Reinforced concrete columns confined by circular spirals and hoops", *ACI Struct. J.*, **90**(5), 542-553.

Shibata, A. and Sozen, M.A. (1976), "Substitute-structure method for seismic design in R/C", *J. Struct. Div. ASCE*, **102**(ST1), 1-18.

Tae, H.K., Dai, J.S. and Hyun, M.S. (2012), "Seismic performance assessment of hollow reinforced concrete and prestressed concrete bridge Columns", *Int. J. Concrete Struct. Mater.*, **6**(3), 165-176.

Takemura, H. and Kawashima, K. (1997), "Effect of loading hysteresis on ductility capacity of reinforced concrete bridge piers", *J. Struct. Eng.*, **43**A, 849-858.

Wei, D.Z. and Wu, H.Z. (2013), "Probabilistic seismic capacity models for RC bridge columns", *Appl. Mech. Mater.*, **353**(356), 2028-2032.

CC